Simultaneous tartrazine-tetracycline removal and hydrogen production in the hybrid electrocoagulation-photocatalytic process using g-C$_3$N$_4$/TiNTAs

Saddam Husein[a], Ryan Rafi Rustamadji[a], Reno Pratiwi[a,c], Eniya Listiani Dewi[b], Slamet[a,*]

[a]Department of Chemical Engineering, Universitas Indonesia, Depok 16424, Indonesia
[b]Research Center for Energy Conversion and Conservation, National Research and Innovation Agency (BRIN), South Tangerang 15314, Indonesia
[c]Department of Petroleum Engineering, Faculty of Earth Technology and Energy, Universitas Trisakti, Jakarta 11440, Indonesia

Abstract

This study aimed to investigate the removal of tartrazine dye & tetracycline antibiotic and hydrogen (H$_2$) production simultaneously through the hybrid electrocoagulation-photocatalytic process using g-C$_3$N$_4$/TiO$_2$ nanotube arrays (TiNTAs) nanocomposite. The g-C$_3$N$_4$/TiNTAs was used as the photocatalyst. The melamine as the precursor of g-C$_3$N$_4$ was varied to obtain the optimal loading on the removal of tartrazine dye & tetracycline antibiotic and hydrogen (H$_2$) production simultaneously. The integrated acrylic photoreactor was equipped with two 250-W mercury lamps. The nanotubular morphology of TiNTAs and nanostructure features of g-C$_3$N$_4$/TiNTAs were examined using FESEM/EDX and HR-TEM/SAED. The XRD patterns indicated the composition of TiNTAs, confirming the presence of anatase and rutile crystalline phases. UV-Vis DRS also showed a redshift in the composite absorbance and a reduced bandgap with g-C$_3$N$_4$ introduction. The results showed that when tartrazine and tetracycline were treated simultaneously, tartrazine was more dominantly degraded compared to tetracycline. In mixed pollutant system condition, the H$_2$ production increased by 17.0% and 41.1% compared to single pollutant system of tartrazine and tetracycline, respectively. The photocatalyst used in the hybrid process was the g-C$_3$N$_4$/TiNTAs (3 g) which provide the optimum H$_2$ production.

Keywords: Tartrazine; tetracycline; g-C$_3$N$_4$/TiO$_2$ nanotube arrays; electrocoagulation; photocatalysis; hydrogen

1. Introduction

Medical waste is a significant threat to both human health and the environment, originating from hospital and WWTP effluents, chemical plants, livestock, and aquaculture sectors [1]. A common medical waste often found is effluent from antibiotics and medicinal dyes, prevalently consisting of tetracycline (C$_{22}$H$_{24}$N$_2$O$_8$) and tartrazine (C$_{16}$H$_9$N$_4$Na$_3$O$_9$S$_2$). In the environment, the low degradation rate and high resistance of tetracycline can lead to the development of antibiotic-resistant microorganisms [2]. Meanwhile, the high solubility of tartrazine in water makes it a common contaminant in hospital effluents, potentially posing adverse effects on human health at high concentrations [3]. Tartrazine dye and tetracycline have the same dangerous potential, but based on the maximum concentration limits in the environment, tetracycline has a lower maximum concentration limit compared to dyes. It indicates that antibiotic waste must be controlled in such a way as to minimize the amount that exceeds the maximum limit. The maximum concentration of dyes is 7.5 mg/kg [4], and the maximum concentration of antibiotics is 0.001 mg/kg [5].

Various process that has been applied to degrade antibiotics and dye wastes include biological, physical, and chemical treatments [6-7]. However, these technologies are only partially effective due to several limitations such as efficiency, energy consumption, and high costs [8].

In addition to medical waste issues, there has been a growing global interest in hydrogen as an alternative energy source. Besides its wide application, hydrogen is an energy source with a significantly high energy density [9-10]. Approximately 96% of hydrogen is obtained from natural gas-based raw materials through steam reforming, electrolysis, and liquid reforming processes, which require high costs and are not environmentally friendly [10]. Consequently, alternative technologies are needed to produce hydrogen without depending on oil- and natural gas-based raw materials.

A promising technology in response to these problems is

* Corresponding author. Tel.: +62 21 7863516; fax: +62 21 7863515
  Email: slamet@che.ui.ac.id

photocatalytic oxidation using TiO$_2$ semiconductors. This technology has gained much attention due to its cost-effectiveness and environmental friendliness in degrading organic and inorganic pollutants in wastewater [7]. TiO$_2$ photocatalysts are also commonly used in photocatalytic water splitting, a process that breaks down water molecules to produce hydrogen and oxygen [11]. However, the large band gap energy of 3.2 eV limits TiO$_2$ in absorbing photons from visible light, confirming its photons absorption from the UV light region. This limitation hampers the efficient use of TiO$_2$ photocatalysts [12] due to the significant ban`d gap value, restricting UV light adsorption to just 4% of sunlight [11].

Previous investigations have focused on two methods to minimize the drawbacks of TiO$_2$. These include the use of TiO$_2$ nanoparticles coated with aluminum to increase the photocatalyst surface area, thereby improving the ability to degrade dye pollutants [13]. Additionally, TiO$_2$ has been developed in nanotube arrays morphology (TiNTAs), characterized by a larger specific surface area, improved photon energy irradiation adsorption, and enhanced electron transport. This structural modification led to a more efficient photocatalytic degradation of dissolved contaminants [14]. In a previous study, the performance of TiNTAs was improved by depositing CuO and other metals, such as Fe, as an electron trapper and reducing the band gap energy of the photocatalyst [15-16]. The modifications successfully lowered the recombination rate of electron-hole pairs and made the photocatalyst more sensitive to visible light irradiation.

g-C$_3$N$_4$ is a photocatalyst with good chemical stability and responsive to visible light due to its lower band gap of 2.7 eV compared to TiO$_2$. However, g-C$_3$N$_4$ has the disadvantage of a relatively high recombination rate of electron-hole pairs [17]. In this study, g-C$_3$N$_4$/TiO$_2$ composites were fabricated to improve the performance of both photocatalysts. To achieve this, TiO$_2$ will be synthesized with nanotube array morphology, facilitating the formation of an effective composite.

In a previous study, a method was developed for wastewater treatment by combining electrocoagulation and photocatalysis in an integrated reactor. The optimal conditions for electrocoagulation, pH, photocatalyst morphology, and photocatalyst dopants were examined to develop a functional system capable of eliminating dissolved pollutants [13–15].

These investigations did not discuss the treatment of more than one type of environmental pollutant. According to [16] the use of the hybrid electrocoagulation-photocatalysis process successfully eliminated methylene blue-ciprofloxacin in a mixed pollutant system. However, other types of multiple pollutants in a mixed system were not investigated extensively.

As electrocoagulation and photocatalytic technologies generate hydrogen during water purification (pollutant removal), efforts to enhance H$_2$ production have led to various modifications. Consequently, this study adds an electrolyte species into the reaction system to evaluate the impact of NaCl on both pollutant removal and hydrogen production within electrocoagulation system.

The electrocoagulation-photocatalysis hybrid process was employed using g-C$_3$N$_4$/TiNTAs to eliminate tartrazine-tetracycline simultaneously, as a wastewater model in a mixed pollutant system and produce hydrogen in an integrated reactor. The incorporation of g-C$_3$N$_4$ onto TiNTAs was achieved using the adsorption method and the loading effect was also analyzed. Photocatalyst characterization was conducted using FESEM/EDX, HR-TEM/SAED, XRD, and UV-Vis DRS. The results were used to examine the effect of specific parameters on tartrazine-tetracycline removal and hydrogen production. Based on the descriptions above, this study aimed to investigate the removal of tartrazine dye & tetracycline antibiotic and hydrogen (H$_2$) production simultanously through the hybrid electrocoagulation-photocatalytic process using g-C$_3$N$_4$/TiO$_2$ nanotube arrays (TiNTAs) nanocomposite. The melamine as the precursor of g-C$_3$N$_4$ was varied to obtain the optimal loading the removal of tartrazine dye & tetracycline antibiotic and hydrogen (H$_2$) production.

2. Materials and Methods

2.1. Synthesis of TiNTAs and g-C$_3$N$_4$/TiNTAs

The titanium plate of 8 cm ✕ 4 cm (Shaanxi Yunzhong Metal Technology Co., LTD) underwent mechanical polishing using 1500 CW sandpaper. The titanium plate was treated with a chemical solution consisting of HF (Merck, 40%), HNO$_3$ (Merck, 65%), and distilled water in a volume ratio of 1:3:46 for 1 minute. Subsequently, the titanium plate was washed with distilled water and sonicated for 20 minutes to completely remove existing impurities.

TiNTAs were synthesized through an anodization process using a glycerol electrolyte solution (P&G Chemicals, 98%), containing 0.5% weight NH$_4$F and 25% volume of water. A pre-prepared platinum mesh and the titanium plate were used as the cathode and anode, respectively, with a voltage of 50 V for 2 h.

g-C$_3$N$_4$/TiNTAs were obtained by depositing g-C$_3$N$_4$ on the TiO$_2$ nanotube arrays surface through an adsorption method. Melamine (Merk analytical, EMSURE® ACS) was used as the precursor for g-C$_3$N$_4$. The TiNTAs plate was sonicated for 30 minutes in a melamine solution with varying concentrations of 1 g, 2 g, and 3 g in 200 mL solvent containing equal parts methanol (Merk analytical, EMSURE® ACS, ISO, Reag. Ph Eur) and water, followed by immersion for 24 h. The samples were air-dried for 30 minutes at room temperature and annealed in an atmospheric furnace at 550°C for 3 h with a heating rate of 3 °C/min to convert melamine into g-C$_3$N$_4$ and enhance its crystallinity. Subsequently, g-C$_3$N$_4$/TiNTAs photocatalyst synthesized using melamine precursors of 1 g, 2 g, and 3 g in 200 mL of solvent were referred to as g-C$_3$N$_4$/TiNTAs (1 g), g-C$_3$N$_4$/TiNTAs (2 g), and g-C$_3$N$_4$/TiNTAs (3 g), respectively.

2.2. Characterizations of g-C$_3$N$_4$/TiNTAs

The morphology and elemental composition of the synthesized photocatalyst samples were analyzed using Field Emission Scanning Electron Microscope (FESEM, Thermo Scientific Quattro S completed with EDS detector) at 30 kV and equipped with Energy Dispersive X-ray spectroscopy (EDX). A Gaussian curve plot was used to determine

nanotube average diameter. Meanwhile, the average nanotube length and wall thickness were measured using the integrated program of the instrument. The nanostructural features were investigated using a High-Resolution Transmission Electron Microscope (HRTEM, FEI Tecnai G2 20 S-TWIN) operating at 200 kV, along with selected area electron diffraction (SAED) analysis.

The crystallite properties were determined using an X-ray Diffraction (XRD) analysis (XRD, Empyrean Series 3 Panalytical) with a copper anode tube (λ = 0.15406 nm) operating at 40 kV and 30 mA. XRD scanning was performed in the 2θ range of 10-60° with step size 2θ of 0.013 and scan step time of 37.995 s. The crystallite size was estimated using the Scherrer equation based on the full-width half maximum (FWHM) method of the XRD peaks. The optical properties and band gap values were determined using the Kubelka-Munk functions from UV-Visible Diffuse Reflectance Spectra (UV-Vis DRS, Agilent Cary 60 UV-Vis Spectrophotometer). The data were obtained in the range of 300-500 nm.

2.3. Characterizations of g-C₃N₄/TiNTAs

The performance tests were carried out in an integrated acrylic reactor for the hybrid electrocoagulation-photocatalysis process. The reactor contained a 500 mL solution of tartrazine (TZ, 20 ppm) and tetracycline (TC, 20 ppm) at pH 11. In the photocatalysis test, an 8 cm x 4 cm g-C₃N₄/TiNTAs photocatalyst was immersed in the pollutant model solution and exposed to illumination from two mercury lamps (17.25% UV and 82.75% visible light, 250 W). Electrocoagulation system was equipped with aluminum (1 mm thick, 8 cm x 4 cm) and stainless steel 316 (2 mm thick, 8 cm x 4 cm) plates as the anode and the cathode, respectively. These electrodes were placed 3 cm apart from each other and connected to a DC power supply (Volomax DC Power Supply KXN-645D). Subsequently, electrocoagulation process performance test was carried out by switching on the power supply at 5 V.

The hybrid electrocoagulation-photocatalytic process performance test was conducted by combining both processes in an integrated acrylic reactor equipped with a stainless-steel mesh to separate electrocoagulation and photocatalysis chamber to prevent the coagulant from entering the photocatalysis chamber and causing a shading effect. The same solution conditions were maintained during this test. Subsequently, the hybrid process experiment was carried out by switching on the mercury lamps and the power supply simultaneously. During the performance test, the solution was stirred continuously, and argon gas flowed through the reactor for 5 min before each experiment to remove oxygen from the system.

Tartrazine-tetracycline samples were taken every 60 minutes throughout the 240-minute experiment. The UV-Vis spectrophotometer (Bell Engineering M51) was used to measure the absorbance of the sample at specific wavelengths. The 392 nm and 237 nm wavelengths were used for measuring the absorbance of tartrazine and tetracycline at pH 11, respectively. To monitor the reduction in concentration of tetracycline and tartrazine, Equation (1) was applied.

$$\%Removal = ((C_o - C)\,/\,C_o) \times 100\% \qquad (1)$$

where C_0 and C represent the concentrations of tartrazine and tetracycline in mg/L (ppm) at the initial and specific time points, respectively. The concentration of hydrogen produced was also analyzed using a Gas Chromatography (Shimadzu GC-2014) equipped with a Molecular Sieve (MS) Hydrogen 5A column, with a known retention time for argon as the carrier gas.

3. Results and Discussion

3.1. Characterization of g-C₃N₄/TiNTAs

FESEM analysis provided a morphological view of the photocatalyst in the form of nanotube arrays immobilized on the surface of the titanium plate with varying loading of g-C₃N₄, as presented in Fig. 1. The results showed that there was no change in the morphology with the introduction of g-C₃N₄ in terms of inner diameter size, wall thickness, and nanotube length. However, nanotube arrays showed very diverse sizes and dimensions.

The calculation of nanotube dimensions, as presented in Table 1, showed an inner diameter ranging from 166 - 193 nm, with a wall thickness of 28 - 37 nm, and a height of 1094 - 1720 nm. These results showed a correlation between g-C₃N₄ loading and changes in nanotube dimensions. Therefore, the addition of g-C₃N₄ loading did not affect the morphology of TiNTAs. The absence of changes in nanotube morphology also showed that the synthesis of TiNTAs through electrochemical anodization was a stable process with consistent results. Furthermore, the unaltered morphology suggested that the main factor affecting the dimensional changes of nanotube was anodization conditions [18]. These included H_2O content influencing nanotube length, fluoride ions affecting diameter, voltage, as well as duration, and stirring conditions during anodization that impacted the homogeneity of the electrolyte solution [19].

Table 1. FESEM/EDX analysis result of the synthesized photocatalysts

Photocatalyst	Average tube inner diameter [nm]	Average tube wall thickness [nm]	Average tube length [nm]	%wt of Elements		
				Ti	O	C
TiNTAs	185 ± 20	29	1094	67.7	32.3	-
g-C₃N₄/TiNTAs (1 g)	190 ± 33	32	1168	67.3	31.7	1.0
g-C₃N₄/TiNTAs (2 g)	168 ± 74	28	1554	66.4	32.3	1.3
g-C₃N₄/TiNTAs (3 g)	166 ± 42	37	1720	65.1	33.5	1.4

The EDX results of the photocatalyst showed an increase in the mass percentage of the C element as the melamine concentration in the precursor solution increased. This showed that a greater concentration of melamine precursor solution yielded a higher amount of g-C₃N₄ that was successfully loaded into TiNTAs. Specifically, when melamine concentrations were 1 g, 2 g, and 3 g in 200 mL of precursor solution, the mass percentages of C were 1.0%, 1.3%, and 1.4%, respectively. The addition of precursor solution ranging from 1 g to 2 g in 200 mL of solvent increased the mass percent of element C by 0.3%, while 2 g to 3 g yielded a 0.1% increase. This showed that the trend of increasing precursor

concentration to the mass percent of the component was a saturation-growth-like relationship. In this pattern, the linearity of the relationship only occurred at lower concentrations and gradually reached a saturation point on the surface of TiNTAs at high melamine concentrations.

Based on the EDX analysis, none of the samples showed the presence of the elemental component N on the photocatalyst surface. This phenomenon occurred because EDX results on pure g-C_3N_4 gave a smaller N element peak compared to the C element. Additionally, in the EDX conducted on g-C_3N_4/TiNTAs nanocomposite, the Ti and O element peaks were significantly intense compared to the C peak. This suggested that the N element was not detected on g-C_3N_4/TiNTAs. The non-detection of N was also reported in a previous study related to EDX analysis of g-C_3N_4/TiO$_2$ nanocomposites [20]. The relatively small loading of g-C_3N_4 on TiNTAs, which remained below 1.5%, contributed to the difficulty in detecting the N element. From the results of FESEM/EDX analysis, g-C_3N_4 loading on TiNTAs did not cause the formation of agglomerations and clusters of g-C_3N_4 particles that could interfere with the active sites of TiNTAs.

The nanostructure of the synthesized photocatalyst was further analyzed using HR-TEM and SAED characterization. The presence and location of g-C_3N_4 loaded on TiNTAs were confirmed. From the TEM analysis results presented in Fig. 2(a), it was discovered that g-C_3N_4 was successfully deposited on TiNTAs, supporting FESEM/EDX analysis. The TEM image also showed that g-C_3N_4 was distributed on the outer wall of TiNTAs.

The HR-TEM analysis presented in Fig. 2(b) and 2(c) showed a crystal structure with interplanar distances of 0.33 nm, 0.32 nm, and 0.35 nm. The distance between two lattice planes of 0.33 nm corresponded to the plane with the hkl value (0 0 2) of g-C_3N_4 component [21]. Meanwhile, the interplanar distance of 0.32 nm and 0.35 corresponded to the plane (1 1 0) of rutile TiO$_2$ crystals and (1 0 1) of anatase TiO$_2$ crystals [22]. Based on the measurement of d-spacing values performed on the SAED diffraction pattern shown in Fig. 2(d), interplanar distance values of 0.3507 nm, 0.2325 nm, 0.1899 nm, and 0.1749 nm were obtained, corresponding to the (1 0 1), (1 1 2), (2 0 0), and (2 0 2) planes of anatase TiO$_2$ crystals, according to JCPDS No. 21-1272 [23]. Additionally, a d-spacing of 0.1355 nm was identified, corresponding to the (3 0 1) plane of rutile TiO$_2$ crystals based on JCPDS No. 21-1276 [24]. In the SAED analysis, no g-C_3N_4 crystals were detected due to the small loading of g-C_3N_4 on TiNTAs, as confirmed in EDX analysis, causing the insignificant diffraction intensity of g-C_3N_4.

The results of the TEM analysis also showed that the diameter of nanotube was getting larger at the bottom. This phenomenon occurred as the anodization duration progressed, causing more TiF$_6^{2-}$ species to dissolve within nanotube wall, and increasing the size of the inner diameter [15]. Consequently, the morphological condition of nanotube becomes a challenge for g-C_3N_4 precursor to enter the interior of nanotube. Based on the results of TEM, HR-TEM, and SAED characterization, it was concluded that the nanocomposite synthesis between g-C_3N_4 and TiNTAs was successfully carried out.
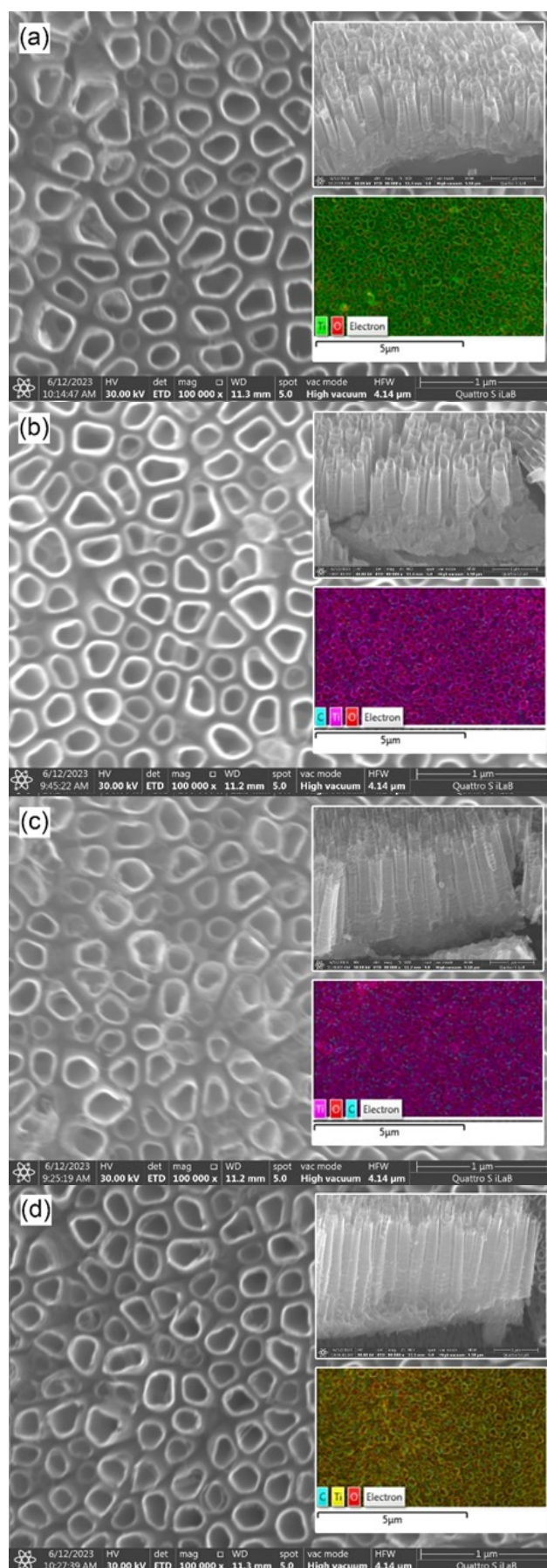

Fig. 1. FESEM Image of (a) TiNTAs, (b) g-C_3N_4/TiNTAs (1 g), (c) g-C_3N_4/TiNTAs (2 g), and (d) g-C_3N_4/TiNTAs (3 g) (Inset: Top: FESEM image from nanotube side, Bottom: EDX elemental mapping)
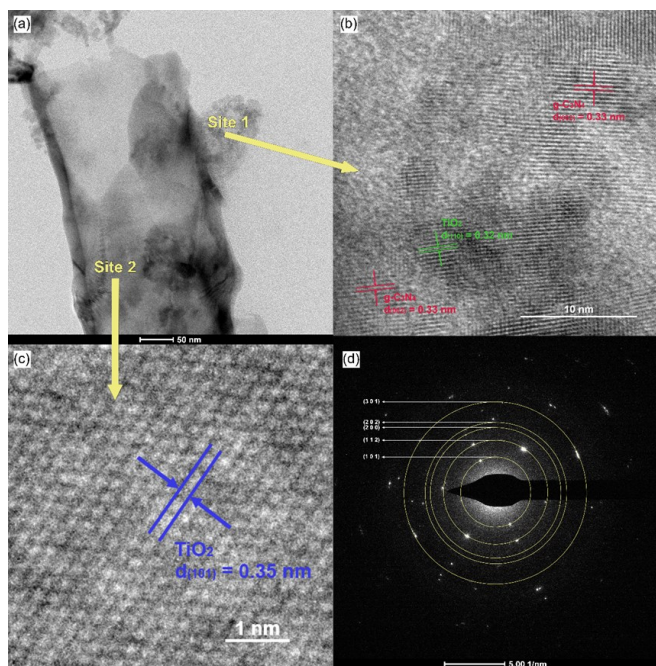
Fig. 2. (a) TEM, (b) & (c) HR-TEM image, and (d) SAED Diffraction Pattern of g-C_3N_4/TiNTAs (3 g)

The XRD patterns in Fig. 3 showed similar diffraction patterns for all photocatalysts. Based on the results, the diffraction peaks of anatase TiO_2 crystals were detected at 2θ = 25.4°, 37.0°, 37.9°, 38.6°, 48.1°, 54.0°, and 55.1°, which corresponded to the (1 0 1), (1 0 3), (0 0 4), (1 1 2), (2 0 0), (1 0 5), and (2 1 1) planes based on JCPDS No. 21 – 1272 [23]. Diffraction peaks of rutile TiO_2 crystals were also detected at 2θ = 27.37°, 36.02°, and 41.16°, corresponding to the (1 1 0), (1 0 1), and (1 1 1) planes based on JCPDS No. 21 – 1276 [24]. Several peaks with high intensity detected at 2θ = 35.2°, 38.5°, 40.3°, and 53.1° corresponded to the (1 0 0), (0 0 2), (1 0 1), and (1 0 2) planes to the titanium metal [25]. Meanwhile, the diffraction peaks of g-C_3N_4 crystal were not detected at 2θ = 12.8° and 27.6°, which corresponded to the (0 0 2) and (1 0 0) planes based on JCPDS No. 87 – 1526 [26].

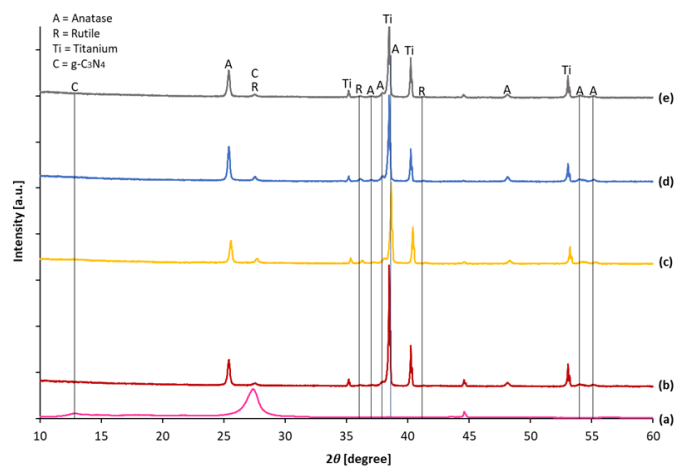Fig. 3. XRD Patterns of a. g-C_3N_4, b. TiNTAs, c. g-C_3N_4/TiNTAs (1 g), d. g-C_3N_4/TiNTAs (2 g), and e. g-C_3N_4/TiNTAs (3 g)

The presence of the rutile crystal phase of TiO_2 was due to the calcination process conducted at a temperature of 550°C for 3 h, with a heating rate of 3°C/minute. The calcination

temperature at 550°C was selected for the optimal conversion of melamine precursor in TiNTAs into g-C_3N_4 [20, 27]. The existence of the rutile crystal phase was also in accordance with the previous study. Based on the results, it was discovered that rutile crystals became evident on TiO_2 when the calcination temperature used was above 500°C [24,28-29]. Consequently, calcination temperatures above 500°C were high enough to promote the growth of rutile crystals.

According to JCPDS No. 87-1526, g-C_3N_4 crystals have two prominent diffraction peaks. Specifically, these peaks are located at 2θ = 27.6°, which corresponds to the (0 0 2) plane due to the stacking of conjugated aromatic layers. A smaller peak is also found at 2θ = 12.8° for the (1 0 0) plane due to the structure of the layered tri-s-triazine unit [30]. However, in all g-C_3N_4/TiNTAs photocatalysts, no diffraction peaks of g-C_3N_4 component were detected. This occurred because of the small amount of g-C_3N_4 loaded into TiNTAs and the low crystallization of melamine, as reported in previous studies [20,27,31].

The small loading of g-C_3N_4 corresponded to the results of EDX characterization. This showed that the mass percentage of the C element in g-C_3N_4/TiNTAs ranged from 1.0 - 1.4%. Additionally, the diffraction of g-C_3N_4 at 2θ = 27.6° peak overlapped with rutile crystal (1 1 0) at 2θ = 27.37°. This made the diffraction peak of g-C_3N_4 challenging to be distinguished from that of rutile crystal (1 1 0). However, the diffraction peak at 2θ = 27.37° for TiNTAs without g-C_3N_4 loading confirmed that the peak at 2θ around 27° for all photocatalyst samples was dominated by the presence of rutile crystals.

The size of the photocatalyst crystallite was calculated using the Scherrer equation. The analysis was carried out using the FWHM (full width at half maximum) method at the main diffraction peak of the anatase crystal at 2θ = 25.4° and the main diffraction peak of the rutile crystal at 2θ = 27.37°. Based on the results, anatase crystal size ranged from 33.0 to 35.7 nm, while rutile crystals varied from 21.7 to 30.0 nm. The composition of both parameters in units of mass percentage was also calculated, with values ranging from 80.9 to 93.5% and 6.4 to 19.1%, respectively. The results for the size and mass fraction of the crystallite in the synthesized photocatalyst are presented in Table 2.

The low amount of g-C_3N_4 loaded on TiNTAs, as evidenced by EDX analysis, suggested insignificant effect on the growth of anatase and rutile crystals during the calcination process. This was shown by the absence of a certain trend between the size and composition of crystals against the amount of g-C_3N_4 loading. Therefore, it can be concluded that g-C_3N_4 loading has no effect on the size and composition of the crystals of the synthesized photocatalyst.

The temperature and duration of the calcination process mainly influenced the size and composition of crystals in the photocatalysts. Generally, an increase in the calcination temperature leads to enhanced crystallinity of the photocatalyst, resulting in a more organized crystal structure, as shown by the sharp and narrow XRD peaks. The crystallite size of all crystal phases also tends to increase with a rise in calcination temperature, showing a higher crystallization process. This shows that the calcination temperature promotes crystalline phase transitions, crystal size enlargement, and

crystallinity of the synthesized photocatalyst [24,32].

Table 2. Crystal size and TiO$_2$ Composition of the synthesized photocatalysts.

Photocatalyst	Crystal size [nm]		TiO$_2$ composition [%wt]	
	Anatase	Rutile	Anatase	Rutile
TiNTAs	33.0	21.7	90.8	9.2
g-C$_3$N$_4$/TiNTAs (1 g)	33.0	29.1	80.9	19.1
g-C$_3$N$_4$/TiNTAs (2 g)	35.7	30.0	88.0	12.0
g-C$_3$N$_4$/TiNTAs (3 g)	34.1	22.6	90.0	10.0

The UV-Vis DRS absorbance spectra presented in Fig. 4 showed a significant shift in the absorbance of TiNTAs towards larger wavelengths. This shift showed an enhancement in the visible light absorption of the synthesized photocatalyst. The decrease in band gap energy of the photocatalyst caused the shift in absorbance from TiNTAs towards visible light with g-C$_3$N$_4$ loading. Furthermore, the determination of the band gap energy of the photocatalyst was achieved by processing the DRS absorbance spectra using the Kubelka-Munk equation and Tauc plot.

The band gap calculation results presented in Fig. 4 showed a 3.28 eV value for TiNTAs, as obtained for TiO$_2$ photocatalysts in a previous study [24, 32]. Furthermore, the loading of g-C$_3$N$_4$ decreased the band gap of the photocatalyst ranging from 3.27 eV to 3.26 eV. This decrease was due to the presence of g-C$_3$N$_4$ semiconductor with a lower band gap (2.7 eV) in the synthesized nanocomposite [33]. The band gap energy of g-C$_3$N$_4$/TiNTAs are located between the TiNTAs (3.28 eV) and g-C$_3$N$_4$ (2.7 eV), as expected. However, the low band gap reduction was due to the small amount of g-C$_3$N$_4$ loaded on TiNTAs, as confirmed by EDX characterization.
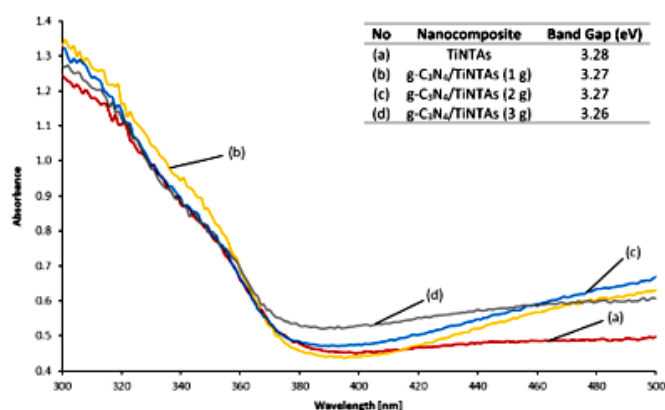

Fig. 4. UV-Vis DRS Spectrum of a. TiNTAs, b. g-C$_3$N$_4$/TiNTAs (1 g), c. g-C$_3$N$_4$/TiNTAs (2 g), and d. g-C$_3$N$_4$/TiNTAs (3 g) (Inset: Band gap values of the photocatalyst)

In TiNTAs photocatalyst without g-C$_3$N$_4$ loading, the majority of the excited electrons and hole pairs from the semiconductor material underwent recombination, which reduced the photocatalysis activity. Therefore, the main goal of compositing g-C$_3$N$_4$ with TiNTAs is to suppress the recombination rate of electron-hole pairs through a charge transfer mechanism between the conduction band and valence band of g-C$_3$N$_4$ and TiNTAs. This process effectively prolongs the lifetime of the charge electron holes, thereby enhancing the photocatalysis activity [31].

3.2. Photocatalytic test on tartrazine degradation and H$_2$ production

Photocatalysis test for 240 minutes showed a significantly low tartrazine degradation, ranging from 2.70 to 3.63%, as presented in Fig. 5 (a). The low level of tartrazine degradation was caused by the high initial concentration of tartrazine, which was 20 ppm, and tartrazine compounds consisting of 16 carbon atoms with 3 carbon rings in their structure. This made tartrazine difficult to degrade through oxidation reactions by photocatalysis. Similarly, Muttaqin et al [16] conducted experiments with an initial concentration of 20 ppm at pH 11 using an optimal photocatalyst of 0.06 M CuO-TNTA at UV lamp irradiation for 12 h and obtained 64% tartrazine degradation. This showed the difficulty of tartrazine compounds to be degraded through photocatalytic reaction.

The performance of H$_2$ production through photocatalysis showed that loading g-C$_3$N$_4$ on TiNTAs significantly increased the amount of H$_2$ gas produced. Photon irradiation for 240 minutes gave H$_2$ gas accumulation of 14.13 μmol/m^2 using TiNTAs, while g-C$_3$N$_4$/TiNTAs (1 g), g-C$_3$N$_4$/TiNTAs (2 g), and g-C$_3$N$_4$/TiNTAs (3 g) photocatalysts yielded accumulation of 22.30 μmol/m^2, 22.63 μmol/m^2, and 26.48 μmol/m^2, respectively. These results showed that loading g-C$_3$N$_4$ on TiNTAs improved the photocatalysis performance regarding H$_2$ production. The profile of H$_2$ accumulation by photocatalysis with a variation of g-C$_3$N$_4$ loading is shown in Fig. 5 (b).
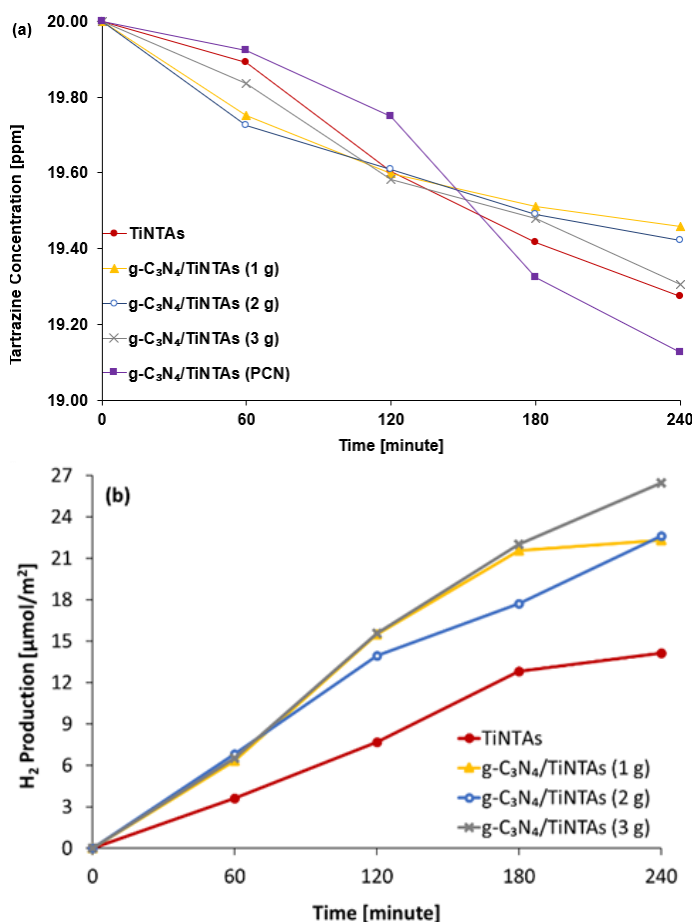

Fig. 5. Effect of g-C$_3$N$_4$ loading on TiNTAs on the a. tartrazine elimination and b. hydrogen production for 240-minute process

The unchanged tartrazine degradation performance and increased H_2 production through photocatalysis with g-C_3N_4/TiNTAs in comparison to TiNTAs can be explained by the formation heterojunction. The synthesized g-C_3N_4/TiNTAs photocatalyst is suspected to form a type-II heterojunction. Semiconductor 1 (g-C_3N_4) has a conduction and valence band with a more negative redox potential position compared to that of semiconductor 2 (TiNTAs). This configuration promotes the migration of electrons from g-C_3N_4 conduction band to TiNTAs. Similarly, holes in the valence band of TiNTAs tend to migrate to that of g-C_3N_4. The accumulation of electrons in the conduction band of TiNTAs and holes in the valence band of g-C_3N_4 facilitates effective charge separation in semiconductor composites through type II heterojunction. Fig. 6a illustrates the charge separation in type II heterojunction, while Fig. 6b shows the mechanism of the •OH attack on tartrazine. This supports the theory that nucleophilic attacks are the first and require a second attack by sulfur-based or electrophilic free radicals such as superoxide radicals (•O_2^-) to break the N=N bond. Production of sulfur-based radicals requires an alkaline solution pH.
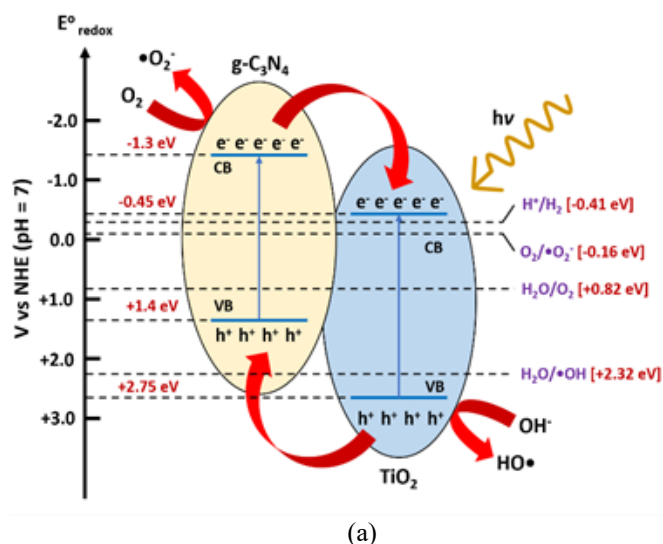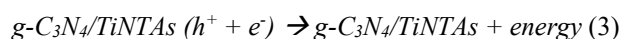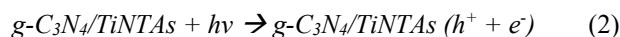

(a)

(b)

Fig. 6. (a) Illustration of charge separation through heterojunction mechanism type-II and (b) detailed proposed mechanism

The limitations of type II heterojunction include low oxidation and reduction ability of the holes and excited electrons. This phenomenon occurs due to charge transfer to the more negative val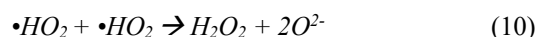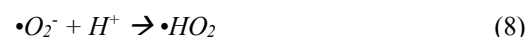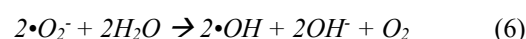ence band and more positive conduction band. However, the effective charge separation compensates for these limitations, clarifying the absence of a decrease in tartrazine degradation performance and higher photocatalytic H_2 production.

The photocatalysis reactions during tartrazine degradation and H_2 production are summarized as follows, regardless of the charge separation mechanisms occurring in the test:
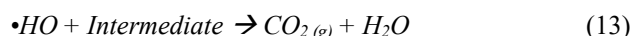
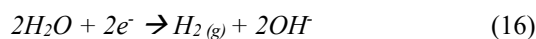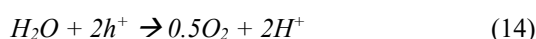Excitation of electrons by photon energy:

$$g\text{-}C_3N_4/TiNTAs + h\nu \rightarrow g\text{-}C_3N_4/TiNTAs\ (h^+ + e^-) \qquad (2)$$

$$g\text{-}C_3N_4/TiNTAs\ (h^+ + e^-) \rightarrow g\text{-}C_3N_4/TiNTAs + energy \quad (3)$$

Formation of radicals and reactive oxygen species:

$$h^+ + H_2O \rightarrow \bullet OH + H^+ \qquad (4)$$

$$e^- + O_2 \rightarrow \bullet O_2^- \qquad (5)$$

$$2\bullet O_2^- + 2H_2O \rightarrow 2\bullet OH + 2OH^- + O_2 \qquad (6)$$

$$\bullet OH + \bullet OH \rightarrow H_2O_2 \qquad (7)$$

$$\bullet O_2^- + H^+ \rightarrow \bullet HO_2 \qquad (8)$$

$$\bullet HO_2 + H^+ \rightarrow H_2O_2 \qquad (9)$$

$$\bullet HO_2 + \bullet HO_2 \rightarrow H_2O_2 + 2O^{2-} \qquad (10)$$

$$e^- + H_2O_2 \rightarrow \bullet HO + \bullet HO \qquad (11)$$

Degradation of tartrazine by radical species:

$$\bullet HO + tartrazine/tetracycline \rightarrow Intermediate \qquad (12)$$

$$\bullet HO + Intermediate \rightarrow CO_{2\,(g)} + H_2O \qquad (13)$$

H_2 production via reaction of water splitting:

$$H_2O + 2h^+ \rightarrow 0.5O_2 + 2H^+ \qquad (14)$$

$$2H^+ + 2e^- \rightarrow H_{2\,(g)} \qquad (15)$$

$$2H_2O + 2e^- \rightarrow H_{2\,(g)} + 2OH^- \qquad (16)$$

3.3. Electrocoagulation Test on Tartrazine Elimination and H_2 Production

Based on the results, electrocoagulation test provides a significant percentage of tartrazine elimination compared to the photocatalysis process. This is because the coagulant from the electrocoagulation process can spread freely in the solution as fine solids. Consequently, the surface area of the coagulant for the adsorption of tartrazine becomes enormous compared to the photocatalyst plate. In this study, electrocoagulation test provided tartrazine elimination of 31.82%, which increased to 59.68% due to the addition of NaCl at 0.2 g/L. H_2 gas accumulation was obtained at 425.57

mmol/m^2 and the incorporation of NaCl at 0.2 g/L caused a 105.03% increase, reaching 872.53 mmol/m^2, as presented in Fig. 7.

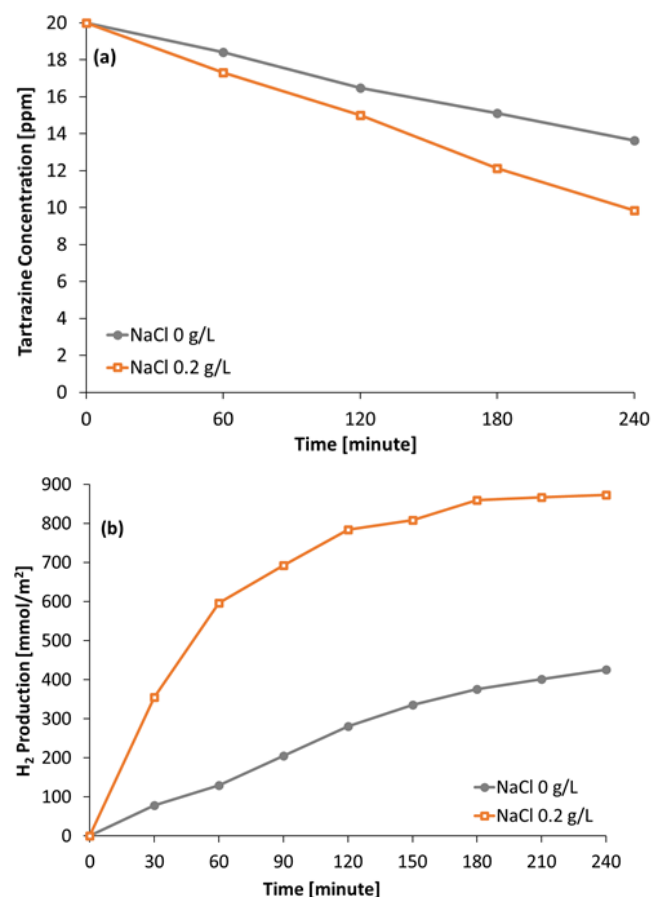electrical resistance is minimized at the same voltage.

Fig. 7. Effect of NaCl addition on the a. tartrazine elimination and b. hydrogen production for 240-minute electrocoagulation process set at a voltage of 5 V
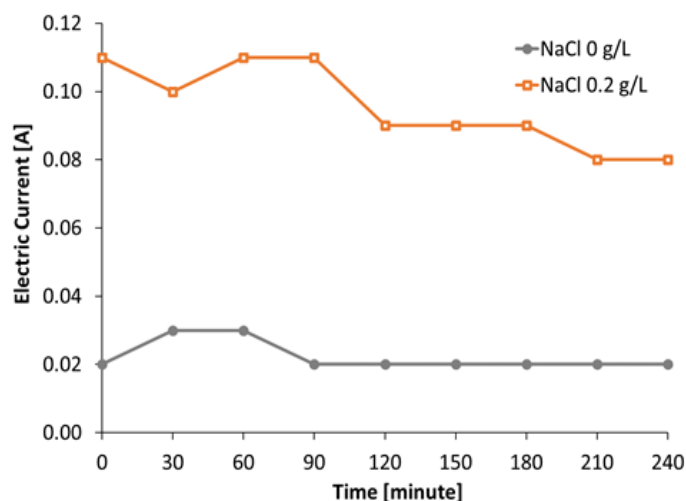

Fig. 8. Electric current profile on NaCl addition

3.4. The hybrid electrocoagulation-photocatalytic process

In the single process of photocatalysis and electrocoagulation test, tartrazine pollutant model was used to obtain optimal g-C$_3$N$_4$ loading on TiNTAs and electrocoagulation conditions for application in the hybrid process. Subsequently, a mixture of tartrazine dye and tetracycline antibiotic as a wastewater model was used in electrocoagulation-photocatalysis hybrid process test to model the presence of more than one type of pollutant in the environment.
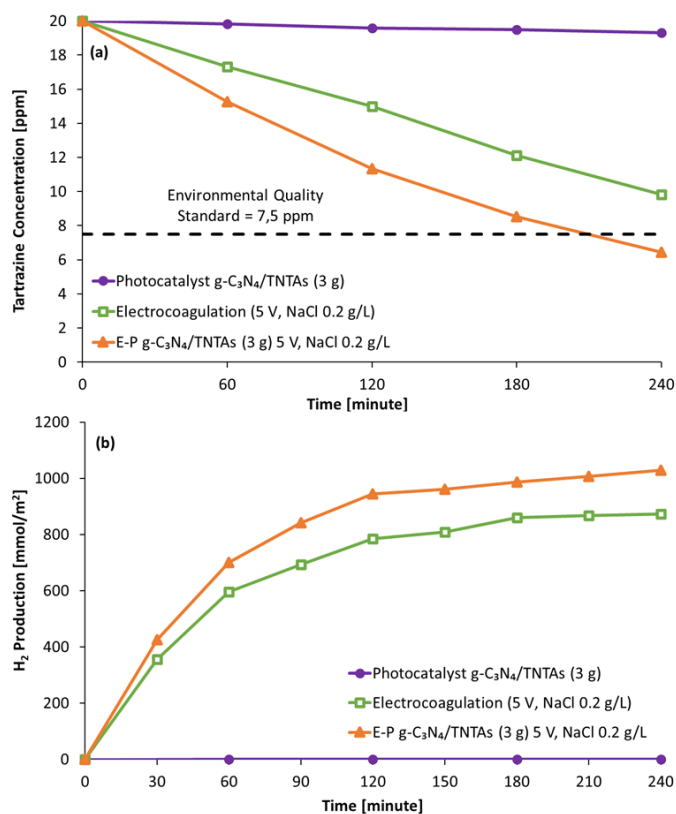
The addition of NaCl to tartrazine solution increased the amount of electric current flowing in electrocoagulation circuit [34] and reduced the electrical resistance of the solution. This showed that there was a change in the solution properties to a strong electrolyte [35]. The addition of NaCl increased the electrical conductivity of the solution. The increase in electric current in electrocoagulation system promotes more Al^{3+} ions to dissolve into tartrazine solution. These Al^{3+} ions react with OH$^-$ ions to form a coagulant to eliminate pollutants. The high consumption of OH$^-$ ions makes the reaction on the cathode shift towards the product, resulting in the generation of abundant electrons. With more electrons on the cathode, a higher rate of water electrolysis reactions occurs, leading to an increase in H$_2$ production [16].

The high conductivity and electric current in electrocoagulation system with the addition of NaCl can be observed from the electric current profile flowing in the system during the test, as presented in Fig. 8. Based on the results, the electric current in electrocoagulation without the addition of NaCl ranged from 0.02 to 0.03 A. Meanwhile, with the addition of NaCl concentration of 0.2 g/L, the electric current flowing ranged from 0.08 to 0.11 A, yielding an average increase of 330%. This corresponds to Ohm's Law, where the electric current flow will be greater when the
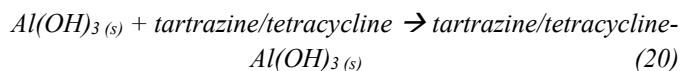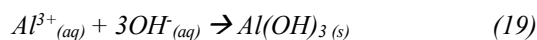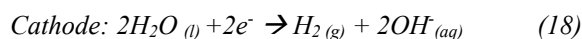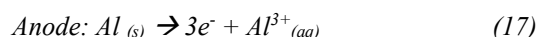

Fig. 9. (a) elimination of tartrazine and (b) hydrogen production as a function of various processes

The degradation of tartrazine by photocatalysis yielded a very small percentage of degradation, which was 3.47%, while electrocoagulation process produced a relatively large percentage of tartrazine elimination at 50.81%. However, the hybrid process resulted in tartrazine elimination of 67.74%, which was greater than the sum of the photocatalysis and electrocoagulation tartrazine elimination. This increase showed a synergistic effect when electrocoagulation and photocatalysis were combined. A similar profile was also found for H_2 gas accumulation in the process variations. Photocatalysis produced H_2 gas at 26.48 mmol/m^2 and electrocoagulation at 872.53 mmol/m^2. Meanwhile, the hybrid electrocoagulation-photocatalysis process was 1,028.16 mmol/m^2. The profiles of tartrazine and tetracycline concentrations and H_2 accumulation in the process variations are presented in Fig. 9.

The enhanced performance of tartrazine elimination in the hybrid process was due to removal of pollutants from two different mechanisms simultaneously. In the hybrid process, tartrazine was degraded by •OH radical species, reactive oxygen species, and holes from photocatalysis reactions. Simultaneously, tartrazine was also adsorbed by Al(OH)$_3$ coagulant from electrocoagulation process. H_2 production in the hybrid system increased because the H_2 generation process occurred in two places. These included water reduction reaction on the cathode surface and water splitting reaction on the photocatalyst surface. In the hybrid process, there was an extensive consumption of OH$^-$ ions for the formation of Al(OH)$_3$ in electrocoagulation process and •OH radicals in the photocatalysis process [36-37]. This intense consumption of OH$^-$ ions led to a decrease in the concentration of OH$^-$. Based on the principle of equilibrium, there was an increase in the number of H$^+$ ions in the reaction system, increasing H_2 production [16].

The reaction that occurs in the anode and cathode in electrocoagulation process is expressed as follows.

$$Anode: Al_{(s)} \rightarrow 3e^- + Al^{3+}_{(aq)} \qquad (17)$$

$$Cathode: 2H_2O_{(l)} + 2e^- \rightarrow H_{2\,(g)} + 2OH^-_{(aq)} \qquad (18)$$

$$Al^{3+}_{(aq)} + 3OH^-_{(aq)} \rightarrow Al(OH)_{3\,(s)} \qquad (19)$$

$$Al(OH)_{3\,(s)} + tartrazine/tetracycline \rightarrow tartrazine/tetracycline\text{-}Al(OH)_{3\,(s)} \qquad (20)$$

The combination of electrocoagulation process with photocatalysis leads to a significant relationship between the two mechanisms. The adsorbent produced from electrocoagulation process becomes less saturated due to the decrease in pollutant adsorption load resulting from the photocatalysis degradation process. Consequently, the adsorption rate of electrocoagulation process becomes higher. In the photocatalysis process, there is a significant decrease in pollutant concentration due to adsorption from electrocoagulation process, significantly reducing the pollutant load that must be degraded. The reduced degradation load will increase the rate of pollutant degradation by photocatalysis. An illustration of the hybrid electrocoagulation-photocatalysis process system is presented in Fig. 10.
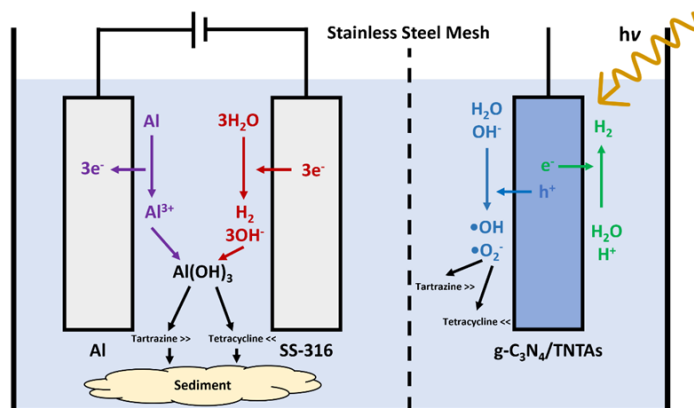

Fig. 10. Illustration of the hybrid electrocoagulation-photocatalysis process

The hybrid process test on a mixed pollutant system gave tartrazine and tetracycline elimination of 70.47% and 20.22%, respectively. Meanwhile, the single pollutant system resulted in the elimination of 67.74% and 54.02%. The elimination was consistently higher for tartrazine pollutants compared to tetracycline for the mixed and single pollutant systems. The elimination selectivity toward tartrazine can be explained by the chemical structure of the pollutants. Tartrazine consists of 16 carbon atoms, while tetracycline comprises 22 carbon atoms. Compounds with more carbon atoms tend to have a highly complex molecular structure. Consequently, the accessibility of degrading agents such as radicals and holes is limited, making the degradation process slower. Tartrazine has a negative charge when dissolved in water which makes it easily neutralized by cationic Al^{3+} species generated from electrocoagulation process. Tetracycline molecules in water do not have a negative charge tendency which makes this compound more difficult to adsorb. The molecular structure of tartrazine and tetracycline is presented in Fig. 11.
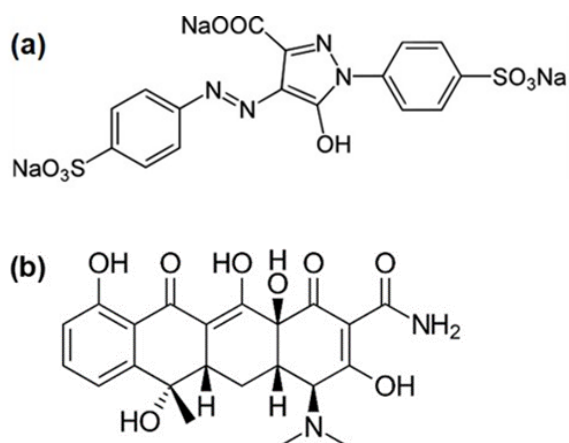

Fig. 11. Molecular structure of a. tartrazine and b. tetracycline

The mixed pollutant system provided H_2 accumulation of 1,203.38 mmol/m^2 with increased hydrogen production of 17.04% and 41.11% compared to single pollutant system of tartrazine (1,028.16 mmol/m^2) and tetracycline (852.82 mmol/m^2), respectively. This higher H_2 production in the mixed pollutant system could be due to the formation of a concentrated solution that promoted photocatalytic degradation reactions. These results are in line with research

reported by Muttaqin et al [16]. Additionally, the adsorption process that occurred in electrocoagulation process was more effective, increasing pollutant elimination and H_2 production. The more intense elimination process in the mixed pollutant system made the consumption of OH^- ions in the solution higher. This phenomenon caused an abundance of H^+ ions in the solution, enhancing the possibility of H^+ ions passing through a reduction reaction to produce H_2 gas both on the photocatalyst and the cathode surface. The concentration profile of tartrazine and tetracycline as well as the accumulation of H_2 in the mixed pollutant system is presented in Fig. 12.

In previous investigations, different results were obtained, where the use of a mixed pollutant model of methylene blue dye and ciprofloxacin antibiotic increased the total removal of both pollutants. In the present study, the introduction of tetracycline into tartrazine solution was beneficial for tartrazine removal and detrimental for tetracycline. This variation in results, depending on the types of pollutants, showed the need for specified mitigation strategies for various environmental pollutants. However, a mixed pollutants system always provides superior H_2 production compared to a single treatment, as reported in a previous study [16]. This variation in results shows the need for further study to optimize electrocoagulation-photocatalysis hybrid process in addressing more than one type of pollutant in the environment.
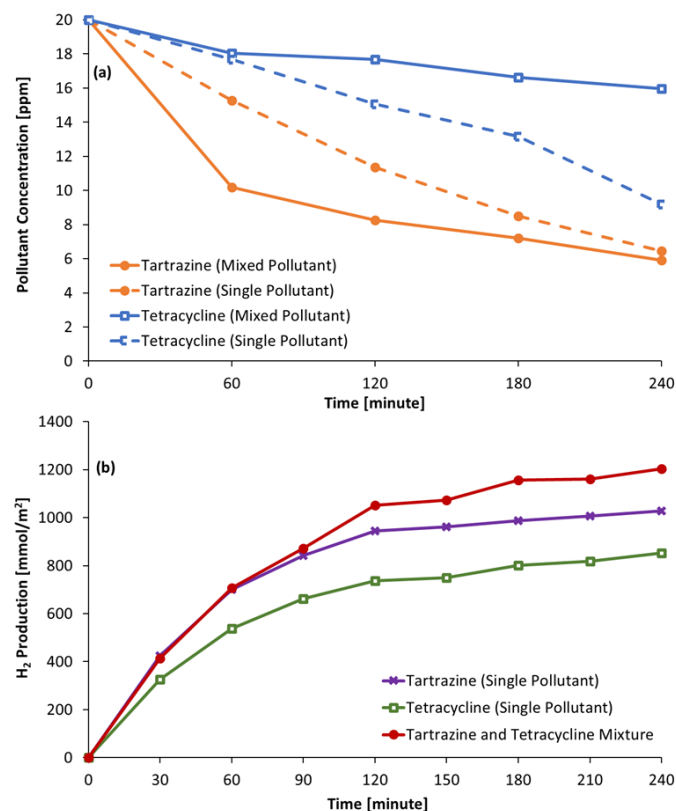
removal of tartrazine dye and tetracycline antibiotic in a mixed pollutant system using a hybrid electrocoagulation-photocatalytic process. The hybrid process provides optimal pollutant elimination and H_2 production compared to the single process, with tartrazine elimination of 67.74% and H_2 production of 1,028.2 mmol/m^2. The significant improvement of the hybrid process suggests a synergetic effect between both processes. When tartrazine and tetracycline were treated simultaneously, the results showed an elimination selectivity towards tartrazine, and the H_2 production increased by 17.0% and 41.1% compared to when tartrazine and tetracycline were eliminated separately. The photocatalyst used in the hybrid process was g-C_3N_4/TiNTAs (3 g), which provides the optimum H_2 production. g-C_3N_4 was successfully composited with TiNTAs, as confirmed by FESEM/EDX and HR-TEM/SAED analysis. Upon g-C_3N_4 introduction, bandgap lowering, and the redshift of the optical onset were also observed. The NaCl-based electrolyte solution was used in the hybrid process to obtain the optimum electrocoagulation condition.

Acknowledgements

Fig. 12. **(a)** elimination of tartrazine-tetracycline and (b) hydrogen production at various pollutants (single and mixture) with the hybrid electrocoagulation-photocatalytic process

4. Conclusion

In conclusion, this study analyzed the simultaneous

References

1. A. C. Singer, H. Shaw, V. Rhodes, and A. Hart, *Review of Antimicrobial Resistance in the Environment and Its Relevance to Environmental Regulators*, Front. Microbiol. 7 (2016) 1-22.

2. M. Cycoń, A. Mrozik, and Z. Piotrowska-Seget, *Antibiotics in the Soil Environment—Degradation and Their Impact on Microbial Activity and Diversity*, Front. Microbiol. 10 (2019) 1-45.

3. K. Rehman, A. Ashraf, F. Azam, and M. S. H. Akash, *Effect of food azo-dye tartrazine on physiological functions of pancreas and glucose homeostasis*, Turkish J. Biochem. 44 (2) (2019) 197–206.

4. J. Silva, R. Fracacio, *Toxicological and ecotoxicological aspects of tartrazine yellow food dye: a literature review,* Revista Brasileira de Ciências Ambientais. (2020) 10.5327/Z21769478746.

5. D. G. J. Larsson, *Antibiotics in the environment,* Ups J Med Sci. 119 (2) (2014) 108-12.

6. V. Vaiano, G. Iervolino, and D. Sannino, *Photocatalytic removal of tartrazine dye from aqueous samples on LaFeO₃/ZnO Photocatalysts*, Chem. Eng. Trans. 52 (2016) 847–852.

7. V. K. Gupta, R. Jain, A. Nayak, S. Agarwal, and M. Shrivastava, *Removal of the hazardous dye—Tartrazine by photodegradation on titanium dioxide surface*, Mat. Scie. Eng. C 30 (5) (2011) 1062–1067.

8. S. Wu, H. Hu, Y. Lin, J. Zhang, and Y. H. Hu, *Visible light photocatalytic degradation of tetracycline over TiO₂*, Chem. Eng. J. 382 (2020) 122842.

9. M. Persson, D. Mignard, and D. Hogg, *Insights on performance and an improved model for full scale electrolysers based on plant data for design and operation of hydrogen production*, Int. J. Hydrogen Energy, 45 (56) (2020) 31396–31409.

10. S.-H. Kim, G. Kumar, W.-H. Chen, and S. K. Khanal, *Renewable hydrogen production from biomass and wastes (ReBioH₂-2020),*

Bioresour Technol. 331 (2021) 125024.

11. M. Ni, M. K. H. Leung, D. Y. C. Leung, and K. Sumathy, *A review and recent developments in photocatalytic water-splitting using TiO₂ for hydrogen production*, *Renew. Sustain. Energy Rev.* 11 (3) (2007) 401–425.

12. M. Sharma, M. K. Mandal, S. Pandey, R. Kumar, and K. K. Dubey, *Visible-Light-Driven Photocatalytic Degradation of Tetracycline Using Heterostructured Cu₂ O–TiO₂ Nanotubes, Kinetics, and Toxicity Evaluation of Degraded Products on Cell Lines*, ACS Omega, 37 (7) (2022) 33572–33586.

13. N. Sharfan, A. Shobri, F. A. Anindria, R. Mauricio, M. A. B. Tafsili, and S. Slamet, *Treatment of Batik Industry Waste with a Combination of Electrocoagulation and Photocatalysis*, Int. J. Technol. 9 (5) (2018) 936-943.

14. S. Slamet and R. Kurniawan, *Degradation of tartrazine and hydrogen production simultaneously with combination of photocatalysis-electrocoagulation*, AIP Conf. Proc. 2024 (2018) 020064.

15. S. Slamet, L. F. Pelawi, M. Ibadurrohman, R. Yudianti, and R. Ratnawati, *Simultaneous Decolorization of Tartrazine and Production of H₂ in a Combined Electrocoagulation and Photocatalytic Processes using CuO-TiO₂ Nanotube Arrays: Literature Review and Experiment*, Indones. j. sci. technol. 7 (3) (2022) 385–404.

16. R. Muttaqin, R. Pratiwi, Ratnawati, E. L. Dewi, M. Ibadurrohman, and Slamet, *Degradation of methylene blue-ciprofloxacin and hydrogen production simultaneously using combination of electrocoagulation and photocatalytic process with Fe-TiNTAs*, Int. J. Hydrogen Energy, 47 (42) (2022) 18272–18284.

17. S. J. Mun and S.-J. Park, *Graphitic Carbon Nitride Materials for Photocatalytic Hydrogen Production via Water Splitting: A Short Review*, Catalysts, 9 (10) (2019) 1-17.

18. Z. Lockman, S. Sreekantan, S. Ismail, L. Schmidt-Mende, and J. L. MacManus-Driscoll, *Influence of anodisation voltage on the dimension of titania nanotubes*, J. Alloys Compd. 503 (2) (2010) 359–364.

19. K. Indira, U. K. Mudali, T. Nishimura, and N. Rajendran, *A Review on TiO₂ Nanotubes: Influence of Anodization Parameters, Formation Mechanism, Properties, Corrosion Behavior, and Biomedical Applications*, J. Bio. Tribocorros. 1 (28) (2015).

20. S. Zhou, S. Liu, K. Su, and K. Jia, *Graphite carbon nitride coupled S-doped hydrogenated TiO₂ nanotube arrays with improved photoelectrochemical performance*, J. Electroanal. Chem. 862 (2020).

21. A. Gashi, *Preparation of g-C₃N₄ based material and analytical characterizations for environmental applications.* Université de Haute Alsace - Mulhouse; The University of Ostrava, 2022. English

22. S. F. Shaikh, R. S. Mane, B. K. Min, Y. J. Hwang, and O. Joo, *D-sorbitol-induced phase control of TiO₂ nanoparticles and its application for dye-sensitized solar cells*, Sci. Rep. 6 (1) (2016) 20103.

23. F. Scarpelli, T. F. Mastropietro, T. Poerio, and N. Godbert, *Mesoporous TiO₂ Thin Films: State of the Art* In *Titanium Dioxide - Material for a Sustainable Environment*, InTech (2018).

24. S. Phromma, T. Wutikhun, P. Kasamechonchung, T. Eksangsri, and C. Sapcharoenkun, *Effect of Calcination Temperature on Photocatalytic Activity of Synthesized TiO₂ Nanoparticles via Wet Ball Milling Sol-Gel Method*, Appl. Sci. 10 (3) (2020) 993.

25. C. Moura, D. Munteanu, L. Cunha, D. G. Constantin, and C. Moura, *The influence of oxygen flow during deposition on the structural, mechanical and tribological properties of titanium oxide magnetron sputtered thin films*, J. Optoelectron. Adv. Mater 14 (11-12) (2012) 964 – 970.

26. M. Karimi-Nazarabad and E. K. Goharshadi, *Highly efficient photocatalytic and photoelectrocatalytic activity of solar light driven WO₃/g-C₃N₄ nanocomposite*, Sol. Energy Mater. *Sol.* Cells, 160 (2017) 484–493.

27. B. Pandey, S. Rani, and S. C. Roy, *A scalable approach for functionalization of TiO₂ nanotube arrays with g-C₃N₄ for enhanced photo-electrochemical performance*, *J. Alloys Compd.* 846 (2020) 155881.

28. J. Bamne, K. Taiwade, P. K. Sharma, and F. Z. Haque, *Effect of calcination temperature on the growth of TiO₂ nanoparticle prepared via sol-gel method using triton X-100 as surfactant*, AIP Conf. Proc. 2039 (2018) 020076.

29. S. Saalinraj and K. C. Ajithprasad, *Effect of Calcination Temperature on Non-linear Absorption Co-efficient of Nano Sized Titanium Dioxide (TiO₂) Synthesised by Sol-Gel Method*, *Mater*. Today Proc. 4 (2) (2017) 4372–4379.

30. H. Azizi-Toupkanloo, M. Karimi-Nazarabad, M. Shakeri, and M. Eftekhari, *Photocatalytic mineralization of hard-degradable morphine by visible light-driven Ag@ g-C₃N₄ nanostructures*, Environ Sci Pollut Res, 26 (30) (2019) 30941–30953.

31. L. Gu, J. Wang, Z. Zou, and X. Han, *Graphitic-C₃N₄-hybridized TiO₂ nanosheets with reactive {001} facets to enhance the UV- and visible-light photocatalytic activity*, J. Hazard Mater. 268 (2014) 216–223.

32. Ratnawati, J. Gunlazuardi, E. L. Dewi, and Slamet, *Effect of NaBF₄ addition on the anodic synthesis of TiO₂ nanotube arrays photocatalyst for production of hydrogen from glycerol–water solution*, Int. J. Hydrogen Energy, 39 (30) (2014) 16927–16935.

33. L. C. Sim, K. S. Koh, K. H. Leong, Y. H. Chin, A. A. Aziz, and P. Saravanan, *In situ growth of g-C₃N₄ on TiO₂ nanotube arrays: Construction of heterostructures for improved photocatalysis properties*, J. Environ. Chem. Eng. 8 (1) 103611.

34. Sutanto, N. Rohadi, and Hidjan, *Impact of Adding Sodium Chloride to Change of Turbidity and Iron Concentration on Treatment Wastewater Using Electrocoagulation Process*, J. Phys. Conf. Ser. 1364 (1) (2019) 012062.

35. S. P. Azerrad, M. Isaacs, and C. G. Dosoretz, *Integrated treatment of reverse osmosis brines coupling electrocoagulation with advanced oxidation processes*, Chem. Eng. J. 356 (2019) 771–780.

36. C. Santoso, Ratnawati, Slamet, *Utilization of glycerol solution for hydrogen production by a combination of photocatalysis and electrolysis processes with Fe-TiO₂ nanotubes,* Commun. Sci. Technol. 8 (2) (2023) 208–215.

37. R. Pratiwi, M. Ibadurrohman, E. L. Dewi, Slamet, A *Novel approachin the synthesis of CdS/titania nanotubes array nanocomposites to obtain better photocatalyst performance.* Commun. Sci. Technol. 8 (1) (2023) 16–24.